

The Magnetic Filling in MAD Simulations and its Impact on the Jet in M87

Felix Glaser¹, Christian M. Fromm^{1,2,3}, Yosuke Mizuno^{4,5,6,7}, Matthias Kadler¹, Karl Mannheim¹

¹ Institute for Physics and Astronomy, University of Würzburg, Emil-Hilb-Weg 31, 97074 Würzburg

e-mail: felix.glaser@stud-mail.uni-wuerzburg.de, christian.fromm@uni-wuerzburg.de

² Institute for Theoretical Physics, Goethe Universität Frankfurt, Max-von-Laue-Str. 1, 60438 Frankfurt, Germany

³ Max-Planck-Institut für Radioastronomie, Auf dem Hügel 69, 53121 Bonn, Germany

⁴ Tsung-Dao Lee Institute, Shanghai Jiao Tong University, Shanghai, 201210, People's Republic of China

⁵ School of Physics and Astronomy, Shanghai Jiao Tong University, Shanghai, 200240, People's Republic of China

⁶ Key Laboratory for Particle Astrophysics and Cosmology (MOE) and Shanghai Key Laboratory for Particle Physics and Cosmology, Shanghai Jiao Tong University, Shanghai 200240, People's Republic of China

⁷ Institut für Theoretische Physik, Goethe-Universität Frankfurt, Max-von-Laue-Strasse 1, D-60438 Frankfurt am Main, Germany

Draft 2.0: February 25, 2026

ABSTRACT

Context. Magnetically arrested accretion disks (MADs) in black hole (BH) jet launching simulations are very successful in modelling low-luminosity active galactic nuclei (AGN) like M87*. The Fishbone-Moncrief (FM) torus is well established for this purpose in numerical astrophysics. The extent of the magnetic vector potential inside the FM torus - that we coin the filling factor - has not been studied before in the case of MAD simulations.

Aims. In detail, we stress the impact on the jet morphology, efficiency and linear polarization imprints of the filling factor as a significant initial parameter of these simulations.

Methods. We employ five 3D general relativistic magneto-hydrodynamics (GRMHD) simulations initialized with large-scale tori, that are immersed in weak, poloidal magnetic fields. To study the impact of the spatial extent of the initial magnetic field, hence the magnetic energy content in the torus, we scale it with the filling factor w.r.t. the poloidal geometric area of the mass density distribution. A common choice of the filling factor is complemented and investigated in terms of altered energetics and angular momentum transport. Further, we investigate the polarized, radiative imprints of synchrotron emission on M87 at 86 GHz, comparing them with Very Long Baseline Interferometry (VLBI) observations. Therefore, we perform general relativistic polarized radiative transfer calculations on the GRMHD data, modelling thermal- and non-thermal electron distributions.

Results. Our simulations show that elevated filling factors significantly increase the electromagnetic (EM) energy contributions and outward angular momentum transport in the jet, due to the initially increased magnetic energy-content in the torus. High magnetic fillings exhibit increased linear polarization fractions, agreeing with the observed $\sim 15\%$ in M87*. We find the jet morphology more prone to disk-vertical flux tubes generated by MAD events. We show, that GRMHD simulations bracket the jet width measurements at the jet base in M87*.

Conclusions. Increased magnetic filling of the FM-torus produces jets that are noticeably brighter downstream compared to our reference models, hence, we find high fillings well suited for extended GRMHD jet models of other low-luminosity AGN, as well.

Key words. black hole physics – magnetohydrodynamics (MHD) – accretion, accretion disks – radiative transfer – radiation mechanisms: non-thermal – globular clusters: individual: M87

1. Introduction

Messier 87 (M87) - a giant elliptical galaxy in the Virgo cluster - provides an important laboratory in the field of extra-galactic jet astrophysics as of many decades. The jet, originating from a compact radio core in the galaxy center, has been studied extensively across the electro-magnetic spectrum ranging from the radio regime up to γ -rays (e.g. Schmitt & Reid 1985; Hada et al. 2013; Kim, J.-Y. et al. 2018; Snios et al. 2019; Acciari et al. 2020; Lu et al. 2023). The EHT Collaboration et al. (EHTC) resolved the radio core of M87* at 1.3 mm employing the very long baseline interferometry (VLBI) technique and interpreted the ring-like structure as the gravitationally lensed synchrotron emission, originating from the accretion disk of a supermassive black hole (SMBH). In more recent observations at 86 GHz, Lu et al. (2023) revealed that the jet and the radio core are in-

deed linked, which was interpreted as the jet base connecting to the accretion flow of relativistic plasma. Super-resolution images of mentioned GMVA observation and VLBA observation at 43 GHz were obtained, employing the resolve algorithm (cf. Kim et al. 2024a,b). The polarimetric EHT observations obtained in 2017 provide viable information on the dynamically important magnetic field structure. From these observations a linear polarization fraction of $\sim 15\%$ (EHT Collaboration et al. 2021a) and an upper bound on the circularly polarized emission fraction of $\langle |v| \rangle < 3.7\%$ (EHT Collaboration et al. 2023) was found. These results constrain theoretical models such as general relativistic magneto-hydrodynamics (GRMHD) simulations of the plasma flow in the vicinity of the black hole. These simulations can be compared to observations by means of general relativistic radiative transfer (GRRT) post-processing calculations

on the GRMHD data. Yang et al. (2024) found the 86 GHz and 43 GHz jet morphology of similar GRMHD simulations to fit the observations very well. Cruz-Osorio et al. (2022) and Fromm et al. (2022) found high spin parameters of $a \sim 0.5 - 0.94$ to be favourable to match the broad-band spectrum and jet morphology of M87* in wide parameter space studies of GRMHD models. In this work we want to focus on the comparison of five 3D GRMHD models and their impact on the electromagnetic footprint of the M87 jet. All share similar initial conditions, but differ with respect to their initial magnetic field configuration. We use the Fishbone-Moncrief (FM) torus (Fishbone & Moncrief 1976) and initialize it with a weak poloidal magnetic field. In most studies, the poloidal extent of the initial magnetic field is set with the offset of the initial vector-potential from a zero-cutoff to 0.80. We compare this model with four simulations that fill the initial torus with varying spatial extents of a weak poloidal magnetic field. These models exhibit drastically altered energetic flux, angular momentum transport properties and jet generation efficiencies. Chatterjee & Narayan (2022) studied the behavior of and drivers for angular momentum transport in magnetically arrested disk (MAD) simulations compared to standard and normal evolution (SANE) simulations in non-spinning BH systems to isolate the side-effects of frame dragging. We complement this study with the case of BHs with high spin and compare the impact of the magnetic filling of the torus. Recent studies by Jacquemin-Ide et al. (2025) complement explanations for the underlying mechanism of MAD-states by studying the inward advective and outward diffusive cycles these simulations exhibit and based on that, derive a first analytical expression for the recurrence timescale of MAD-states. Further parametrical investigation of the MAD-setup by Cho & Narayan (2025) found that the overall variability in the simulations is sensitive to the ratio of rotational and magnetic energy in the initial setup, which connects well to our study, where we tune the initial magnetic energy content.

This paper contains two major parts: In Sec. 2 we introduce the underlying GRMHD equations and simulation setups. We conduct tests on the resolution of the magneto-rotational instability (MRI). Thereafter, we study the differences in the jet energetics and will then determine the efficiency of the energy extraction from the BH and disk to the energy flux in the jet. We connect this analysis further with the investigation of the angular momentum transport of the five simulations. Connecting to the morphological study of the radiative properties of a subset of three simulations in Sec. 3, we consider the impact of magnetic flux eruptions from the BH on the hydrodynamical jet structure, of these simulations. In Sec. 3 we ray-trace the polarized synchrotron emission from a population of thermal and non-thermal electrons asserted to the GRMHD simulations. After the ray-tracing setup is introduced, we will compare the jet morphology at 86 GHz and present spatially resolved, as well as time-dependent linear polarization fractions. Next we compare the jet edge and width profiles of the three different models with observations of (Lu et al. 2023) and discuss the impact of flux eruptions on the synchrotron emission from the jet and disk.

2. General Relativistic Magneto-Hydrodynamics

We employ the 3D GRMHD code *Kokkos-based High-Accuracy Relativistic Magnetohydrodynamics with AMR* (KHARMA; Prather et al. (2021); Prather (2024)), that simulates accretion onto and jet launching from black holes. KHARMA solves the ideal, non-radiative MHD equations on curved space-times with four-metric $g_{\mu\nu}$ and metric determinant g in geometric units ($G =$

$c = 1$ and a factor of $1/\sqrt{4\pi}$ is absorbed in the magnetic field). Throughout this paper we will use the code units for the time- and length-scales, i.e. the light-crossing time is redifend to $t_g = 1 G_N M_{\text{BH}}/(c^3) \equiv 1 \text{ M}$ and the gravitational radius is $r_g = 1 G_N M_{\text{BH}}/(c^2) \equiv 1 \text{ M}$, where G_N is Newton's constant, c is the vacuum speed of light, M_{BH} is the BH mass and M is the mass unit that scales the units in the simulations. Greek indices run through (0, 1, 2, 3) and Roman indices through (1, 2, 3) and we make use the Einstein summation convention. We use a Kerr black hole solution on a modified spherical coordinate system (Funky-Modified-Kerr-Schild-coordinates; FMKS). These coordinates exhibit a decreasing grid cell size in θ -direction towards the equator ($\theta = \pi/2$), that become increasingly cylindrical along the jet-axis ($\theta = 0$ and $\theta = \pi$). The radial extent of the cells increase exponentially, therefore high resolution is given at small radii, where finely resolving the accretion process is vital. (r, θ, ϕ) refer to the ordinary spherical coordinates. The simulation grids are equal in all simulations, where we employ $N_r = 256$, $N_\phi = 128$ and $N_\theta = 128$ cells in the respective directions. The radial boundaries range from $r = (1.1659 - 1000) \text{ M}$, and otherwise use the complete map in $\phi = (0 - 2\pi)$ rad and $\theta = (0 - \pi)$ rad. The underlying equations solved by KHARMA are the covariant conservation of mass, local conservation of energy-momentum and the covariant Maxwell equations (cf. Mizuno & Rezzolla (2024) for more details on the derivation):

$$\nabla_\mu(\rho u^\mu) = 0; \quad \nabla_\mu T^{\mu\nu} = 0; \quad \nabla_\mu {}^*F^{\mu\nu}. \quad (1)$$

ρ denotes the rest-mass density and u^μ the four-velocity. ${}^*F_{\mu\nu}$ is the dual Faraday tensor and the stress-energy tensor is defined in the case of ideal MHD as follows:

$$T^{\mu\nu} = (\rho h_{\text{tot}}) u^\mu u^\nu + \left(p + \frac{1}{2} b^2 \right) g^{\mu\nu} - b^\mu b^\nu, \quad (2)$$

with total specific enthalpy $h_{\text{tot}} = h + b^2/\rho$ and fluid pressure p . The magnetic field four-vector b^μ in its temporal component and spatial components reads:

$$b^t = \frac{\Gamma(B^i u^i)}{\alpha}; \quad b^i = \frac{(B^i + \alpha b^2 u^i)}{\Gamma}, \quad (3)$$

where B^i is the magnetic field three-vector measured by an Eulerian observer, α the lapse function and Γ the bulk Lorentz factor. Note, that with the definition of b^μ in Eq. (3), we make use of the notation $b^2 = b^\mu b_\mu$ in Eq. (2). We use the plasma-beta $\beta = p/b^2$ and magnetization $\sigma = b^2/\rho$ parameters for diagnostics with:

$$b^2 = \frac{B^2 + \alpha^2 (b^t)^2}{\Gamma^2} = \frac{B^2}{\Gamma^2} + (B^i v_i)^2 \quad (4)$$

The system of equations is closed by an equation of state. We assume an ideal gas, that relates the enthalpy h to the pressure p and density ρ :

$$h = 1 + \frac{\hat{\gamma} p}{(\hat{\gamma} - 1)\rho}, \quad (5)$$

with the adiabatic index $\hat{\gamma}$ (Antón et al. (2006)).

We employ inflow and outflow boundary conditions in a radial coordinate, along the polar boundaries we use a solid reflective wall (Olivares et al. (2019)). In the azimuthal direction we employ periodic boundary conditions to all physical quantities across the cells at $\phi = 0$. The GRMHD equations are solved with finite-volume and high-resolution, shock-capturing methods, that are the Lax-van Leer Friedrichs (LLF) flux formula

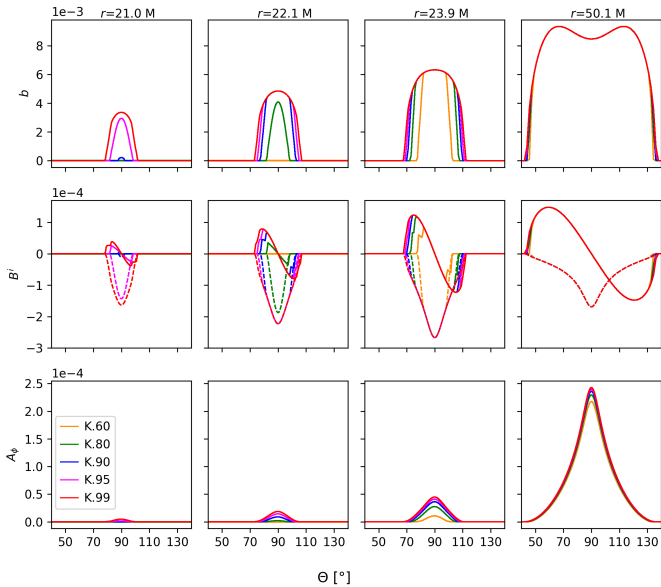


Fig. 1. Invariant magnetic field strength b , the spatial magnetic field components B^r and B^θ , and four-vector-potential component A_ϕ over the polar angle at the initialization step ($t = 0$ M). Colors correspond to simulations K. 60 (orange), K. 80 (green), K. 90 (blue), K. 95 (magenta) and K. 99 (red). In the middle row the solid lines show B^r and the dashed lines B^θ . We choose polar slices at radii around the inner edge of the torus at $r_{\text{in}} = 20$ M and at the pressure maximum in the tori at $r = 50$ M. Note that going from left to right columns, i.e. radially outwards, the simulations with higher filling factors show increased magnetic field strengths and extended magnetic field, both radially and in the polar-angle, especially at the inner edge of the torus.

in combination with the WENO5 reconstruction scheme and in synchronization with the IMEX scheme. The density floor is set to $\rho_{\text{min}} = 10^{-6}$, the internal energy floor to $u_{\text{min,geo}} = 10^{-8}$, the ceiling of the magnetization is $\sigma_{\text{max}} = 100$ and the ceiling of the internal energy is $(u/\rho)_{\text{max}} = 2$. The initial pressure maximum in the torus is set to $\rho_{\text{max}} = 1$. The 3D GRMHD simulations are initialized with a magnetized torus in hydrodynamic equilibrium with a rotating Kerr BH in the center of the simulation domain. Here, we use a setup that allows the disk to partially become magnetically arrested. In the MAD setup we add a single poloidal loop in the vector potential on top of the FM torus (Fishbone & Moncrief (1976)) in the following way:

$$A_\phi \propto \max(q - (1 - F), 0), \quad (6)$$

with

$$q = \frac{\rho}{\rho_{\text{max}}} \left(\frac{r}{r_{\text{in}}} \right)^3 \sin^3 \theta \exp\left(\frac{-r}{400}\right), \quad (7)$$

We solely vary the filling factor F throughout the simulations from 0.6 – 0.99, keeping other initial conditions of the GRMHD simulations constant. Those are constant adiabatic index $\hat{\gamma} = \frac{5}{3}$, inner radius $r_{\text{in}} = 20$ and radius of the density maximum $r_c = 41$ of the torus as well as the dimensionless spin parameter $a = 15/16$ of the BH. The plasma-beta is initialized such that its minimal value is above $\beta_{\text{min}} = 2\nu/b^2 = 100$. We refer to the five models as K. 60, K. 80, K. 90, K. 95 and K. 99 corresponding to the simulations in that the filling factor is set to $F = 0.60$, $F = 0.80$, $F = 0.90$, $F = 0.95$ and $F = 0.99$, respectively. In Appendix A we present more details on the correspondance of the filling factor to the volumes initialized with magnetic field relative to

the torus volume.

In Eq. (6), the effect of F is to proportionally scale the off-set from the zero cut-off of A_ϕ , that is visible in the bottom row of Fig. 1. With increasing F , the off-set of A_ϕ increases, which in turn increases the poloidal extent, or to be precise, the total volume containing cells that have non-zero magnetic field values. For further details we refer to Appendix A, where we also address that the filling factor does not scale the poloidal-field extent linearly to the extent of the torus, it is rather close to the latter and for $F \gtrsim 0.80$ above it (cf. Appendix Tab. A.1).

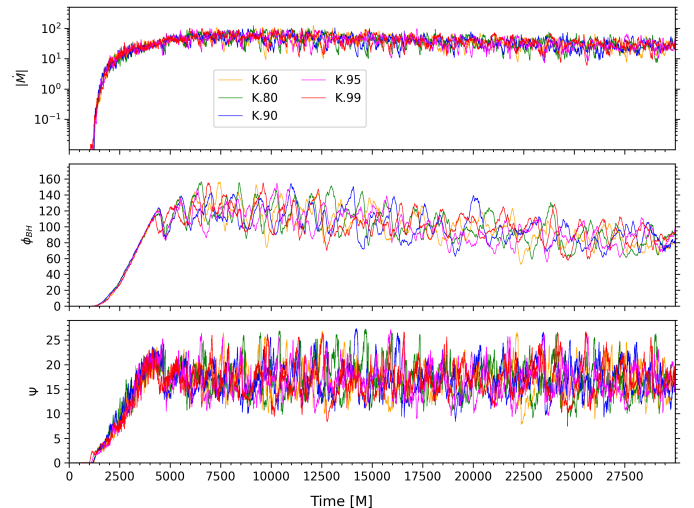


Fig. 2. Mass accretion rates \dot{M} , magnetic flux through the event horizon of the BH ϕ_{BH} and the MAD-parameter $\Psi = \phi_{\text{BH}}/\sqrt{\dot{M}}$ for the simulations K. 80, K. 90 and K. 99 over time.

All simulations are calculated up to a simulation time of 30000 M. We show the mass accretion rate \dot{M} , the magnetic flux through the event horizon ϕ_{BH} and the MAD-parameter $\Psi = \phi_{\text{BH}}/\sqrt{\dot{M}}$ over the full temporal range of the simulations in Fig. 2.

In Appendix B Fig. B.1 we present azimuthal and time-averaged cross-sections of the meridional plane of ρ , σ , magnetic field magnitude $b = \sqrt{|b_\mu b^\mu|}$, plasma- β and ion temperature Θ_i .

2.1. Resolution and MRI Suppression Tests

In this section we investigate the resolution of the magneto-rotational instability (MRI), which is thought to be the main driver of angular momentum and energy transport of plasma accretion in SMBHs systems. Due to the limitations of finite resolution, the spectrum of MRI modes is truncated in simulations, hence is able to produce various numerical artifacts. Truncation of the MRI modes affects the wavenumber range of turbulence modes caused by the MRI, and consequently alters the rate at which nonlinear mode-mode couplings transfer energy from large- to small-scale dynamics. Insufficient resolution of the fastest growing MRI mode brings the turbulent field amplification to a halt and numerical dissipation takes over, hence the field decays. We test whether underlying MRI modes are well resolved by the physical criterion, that the number of grid-cells that are able to capture the MRI wavelength λ_{MRI} is sufficiently large. The so-called quality- or Q -factors (see Sano et al. (2004); Noble et al. (2010); Porth et al. (2019)) are defined to reflect the resolution of the underlying MRI mode with the grid spacing in

a given spatial direction $\Delta x^{(i)}$:

$$Q^{(i)} \equiv \frac{\lambda_{\text{MRI}}^{(i)}}{\Delta x^{(i)}}. \quad (8)$$

The wavelength of the fastest growing MRI mode and the cell extent in a given direction can be defined as:

$$\lambda_{\text{MRI}}^{(i)} \equiv \frac{2\pi}{\sqrt{(\rho h + b^2)\Omega}} b^\mu e_\mu^{(i)}, \quad \Delta x^{(i)} \equiv (\Delta x^\mu)^{(i)} e_\mu^{(i)}. \quad (9)$$

$\Omega = u^\phi/u^t$ is the azimuthal angular velocity of the fluid measured in the locally non-rotating reference frame (LNRF) in Kerr-spacetime and $e_\mu^{(i)}$ is the tetrad basis one-form, where the LNRF is boosted into the comoving frame of the fluid (cf. Takahashi 2008, for the basis transformations). $\Delta x^{(i)}$ is the grid spacing in a fluid frame tetrad basis oriented along the LNRF. $(\Delta x^\mu)^{(i)}$ is a vector containing for each i one of the grid spacings in Kerr-Schild coordinates. For the θ -coordinate and grid spacing $\Delta\theta$ in Kerr-Schild this would look like the following: $(\Delta x^\mu)^{(\theta)} = (0, 0, \Delta\theta, 0)^T$ and is analogously calculated for the other coordinates (r, ϕ) . We calculate the Quality factors Q^r , Q^θ and Q^ϕ and average them over a region that includes the wind and disk regions, which is defined by the bounds $\pi/3 \geq \theta_{\text{disk}} \geq 2\pi/3$ and radial upper bound $r_{\text{disk}} \leq 50 M$, where we always take the full azimuthal map of $0 \geq \phi > 2\pi$. The spatial average is calculated as the expectation value over the covariant volume as follows:

$$\langle Q^{(i)} \rangle_w = \frac{\iiint \sqrt{-g} dr d\theta d\phi Q^{(i)}(r, \theta, \phi) w(r, \theta, \phi)}{\iiint \sqrt{-g} dr d\theta d\phi w(r, \theta, \phi)}, \quad (10)$$

where $w(r, \theta, \phi)$ is a weighting function that acts as a masking function. In the case of the disk averages this function is 1 inside the poloidal bounds specified above and 0 outside.

We show the temporal evolution of the disk averaged quality-factors and their median values in Appendix D Fig. D.1. Sano et al. (2004) suggested Q -factors of $Q > 6$ to correspond to sufficient resolution of the MRI. We match these requirements in $Q^{(\theta)}$ and $Q^{(\phi)}$ with consistent values in all simulations with median values in time of $Q_{\text{med}}^{(\theta)} \gtrsim 35$, $Q_{\text{med}}^{(\phi)} \gtrsim 12$ and time averages of $\langle Q^{(\theta)} \rangle_t \gtrsim 60$, $\langle Q^{(\phi)} \rangle_t \gtrsim 16$ valid for all simulations over the time span ranging from [10000, 30000] [M] (exact values are shown in Fig. D.1 and meridional snapshots in Appendix D Fig. D.2).

2.2. Electromagnetic and Kinetic Energy Flux in the Jet

For the time-series analysis, presented henceforth, we estimate the error of all time-averaged quantities by means of the correlation error σ_{corr} (cf. Appendix E for the formula and more details). This takes into account that the number of data points that are independent of one another is reduced if the data is correlated. The total energy flux is determined via the energy momentum tensor from Eq. (2) by contraction with the metric tensor and reformulating the enthalpy in terms of the internal energy density $u = v/(\hat{\gamma}-1)$ to be

$$T_\mu^\nu = (\rho + \hat{\gamma}u + b^2) u^\nu u_\mu - b^\nu b_\mu + (p + b^2/2) \delta_\mu^\nu \quad (11)$$

$$= (\rho + p + u + b^2) u^\nu u_\mu - b^\nu b_\mu + (p + b^2/2) \delta_\mu^\nu, \quad (12)$$

where δ_μ^ν is the Kronecker delta. The sub tensor responsible for the EM contribution to the r - t component is

$$T_{\text{EM}t}^r = b^2 u^r u_t - b^r b_t. \quad (13)$$

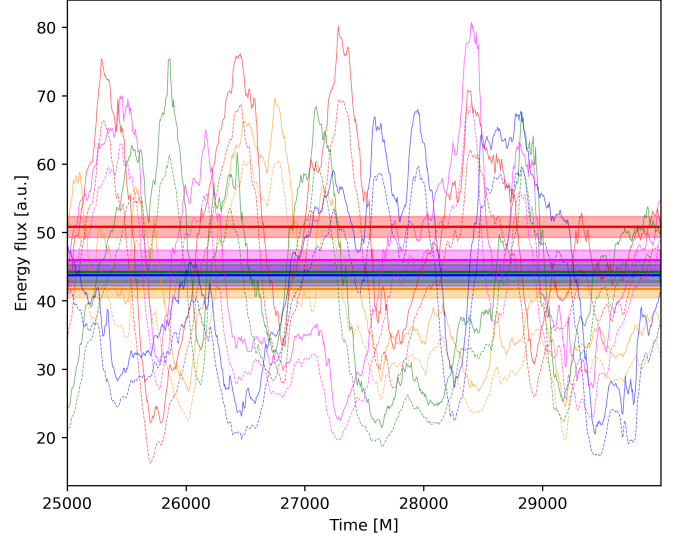


Fig. 3. Temporal evolution of the total energy flux (solid lines) and EM energy flux (dashed lines) measured at $r = 10 M$ in the jet for simulations K. 60 (orange), K. 80 (green), K. 90 (blue), K. 95 (magenta) and K. 99 (red). The horizontal lines show the average of the total energy fluxes for each run over the shown time interval.

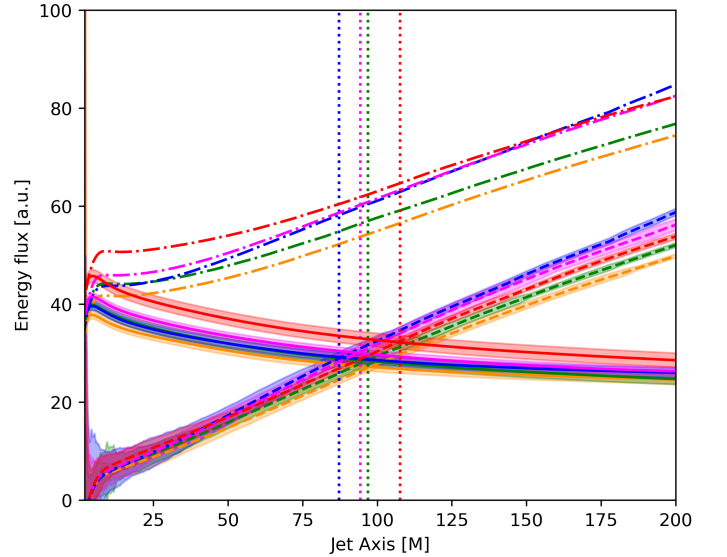


Fig. 4. Time averaged total energy fluxes (dash-dotted lines), EM energy fluxes (solid lines) and kinetic energy fluxes (dashed lines) in the time interval (25000 – 30000) M for varying BH separations along the jet for simulations K. 60 (orange), K. 80 (green), K. 90 (blue), K. 95 (magenta) and K. 99 (red). The vertical dotted lines indicate the radii at which the kinetic and EM energy fluxes are in equipartition.

And analogously the sub tensor for the kinetic contributions is

$$T_{\text{Kin}t}^r = (\rho + p + u) u^r u_t. \quad (14)$$

The total, EM and kinetic energy fluxes are then determined by

$$\dot{E} = - \iint \sqrt{-g} d\theta d\phi T_t^r \quad (15)$$

$$\dot{E}_{\text{EM}} = - \iint \sqrt{-g} d\theta d\phi T_{\text{EM}t}^r \quad (16)$$

$$\dot{E}_{\text{Kin}} = - \iint \sqrt{-g} d\theta d\phi T_{\text{Kin}t}^r \quad (17)$$

Before executing the integral we impose the condition that the Bernoulli parameter has to be > 1.02 , corresponding to the outflowing part of the plasma shown by the area inside the contours in the bottom row of Fig. 10. We further calculate the energy fluxes at varying radial coordinates and times.

In Fig. 3 we show the time dependence of the total and EM energy flux calculated at a fixed radius $r = 10 M$. K. 99 on average exhibits a significantly higher energy flux of ~ 50 [a.u.] exceeding the other simulations by $\geq 3\sigma_{\text{corr}}$, directly boosting the efficiency of the jet launching, due to the comparable mass accretion rates over all simulations. The energy flux at the jet base is highly dominated by the EM part of the energy flux ($\sim 87\%$) for K. 99 and causes the total energy flux excess. The dependence of the time-averaged total energy flux through the jet on the distance from the BH along the jet parallel axis can be taken from Fig. 4. The EM and kinetic contributions are in equipartition at different distances from the BH (vertical dashed lines) for each simulation. This is especially evident for simulation K. 99, being significantly more electromagnetically dominated both in extent along the jet and magnitude. We note, that the energy fluxes increase with BH separation along the jet, since plasma from the wind region becomes gravitationally unbound, i.e. it reaches $hu_t > 1.02$.

2.3. Outflow Efficiencies

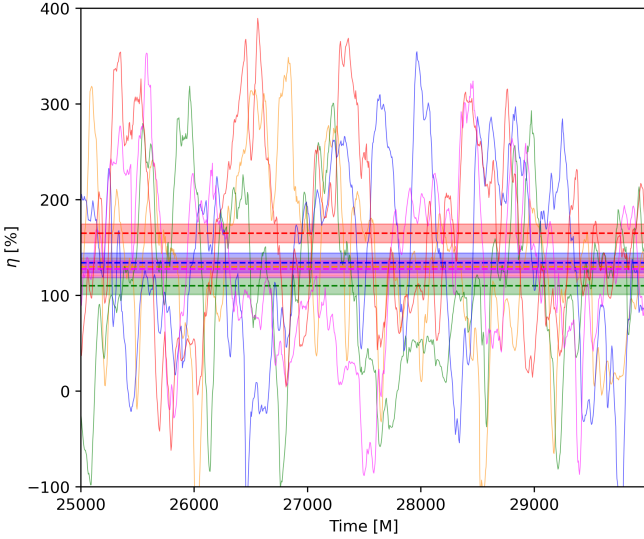


Fig. 5. Jet efficiencies for simulations K. 60 (orange), K. 80 (green), K. 90 (blue), K. 95 (magenta) and K. 99 (red), where the dashed horizontal lines show the time averaged efficiencies and the correlation corrected $2\sigma_{\text{corr}}$ error-band over the shown interval (listed in Tab. 1).

We define the efficiency of energy extraction from the BH spin and disk to outflowing energy at the poles as follows:

$$\eta = \frac{\dot{M}_{5M} - \dot{E}}{\langle \dot{M}_{5M} \rangle}, \quad (18)$$

where we make use of Eq. (15) and calculate the mass accretion rate at $r = 5 M$, \dot{M}_{5M} , and its average $\langle \dot{M}_{5M} \rangle$ over the time interval $t = [25000, 30000] M$. This time-interval is best suited, as the accretion disk is well converged into a steady-state. This can be seen by the mass-accretion rate decelerating its decline towards the end of the simulations (cf. Fig. 2). For comparison,

we also show \dot{M}_{5M} in the beforementioned interval in Appendix Fig. C.1. The nearly identical average mass-accretion rates as well aid the comparison of the efficiencies (see Eq. (18)).

We explicitly do not use the mass accretion rate at the event horizon \dot{M} (compare Fig. 2), but instead calculate the flux at $5 M$ since this excludes the injected matter to set the density floor at the inner simulation boundary. The radial rest-mass energy density flux is defined as follows:

$$\dot{M}_{5M} = \iint_{r=5M} \sqrt{-g} d\theta d\phi \rho u^r \quad (19)$$

The resulting efficiencies of the energy extraction process in all three models are shown in Fig. 5. On average the K. 99 simulation exhibits a vastly improved efficiency of $\sim 60\%$ excess compared to the commonly used MAD-setup K. 80. The averages, errors and peak values of all simulations can be found in Tab. 1.

Simulation	$\langle \eta \rangle$ [%]	max(η) [%]
K. 60	129.8 ± 9.2	348.7
K. 80	110.0 ± 9.0	318.6
K. 90	134 ± 10	355
K. 95	127.5 ± 8.7	353.2
K. 99	164.9 ± 9.7	390.0

Table 1. Time-averages, corresponding error and maxima of efficiencies in the time interval $t = \{25000 M - 30000 M\}$ for each GRMHD simulation (cf. Fig. 5).

2.4. Angular Momentum Transport

In the following section, we investigate the angular momentum transport, by that linking it to the jet efficiency as well as to the impact of the magnetic energy content in the torus on the dynamics from the initialization of the simulations. Following the approach and definitions of the angular momentum fluxes of Chatterjee & Narayan (2022), we define the radial component of the time averaged and shell-integrated angular momentum flux vectors \mathbf{J}^i ($i \in (r, \theta)$), accordingly. The total flux is defined as

$$\mathbf{J}_{\text{tot}}^i = \langle T_{\phi}^i \rangle_{t,\phi}, \quad (20)$$

the advective flux reads

$$\mathbf{J}_{\text{adv}}^i = \left\langle (\rho + u_g + b^2/2) u^i \right\rangle_{t,\phi} \langle u_{\phi} \rangle_{t,\phi}. \quad (21)$$

The stress induced flux is given by

$$\mathbf{J}_{\text{stress}}^i = \mathbf{J}_{\text{tot}}^i - \mathbf{J}_{\text{adv}}^i, \quad (22)$$

which can be further subdivided into the flux induced by Maxwell-stresses

$$\mathbf{J}_{\text{stress,M}}^i = \langle b^2 u^i u_{\phi} / 2 - b^r b_{\phi} \rangle_{t,\phi}, \quad (23)$$

and by Reynolds-stresses, which are subdominant and therefore do not add to the discussions in this paper, hence $\mathbf{J}_{\text{stress}}^i \sim \mathbf{J}_{\text{stress,M}}^i$. We time-average the quantities again over the interval $t = [25000, 30000] M$ in order to compare it with the jet energetics and efficiencies from the previous Sec. 2.2 and Sec. 2.3.

In Fig. 6 we present the polar and radial dependence of time- and azimuthally averaged angular momentum transport. In the left panel we show the time- and azimuthally averaged total angular momentum vector-field for the first time for simulations

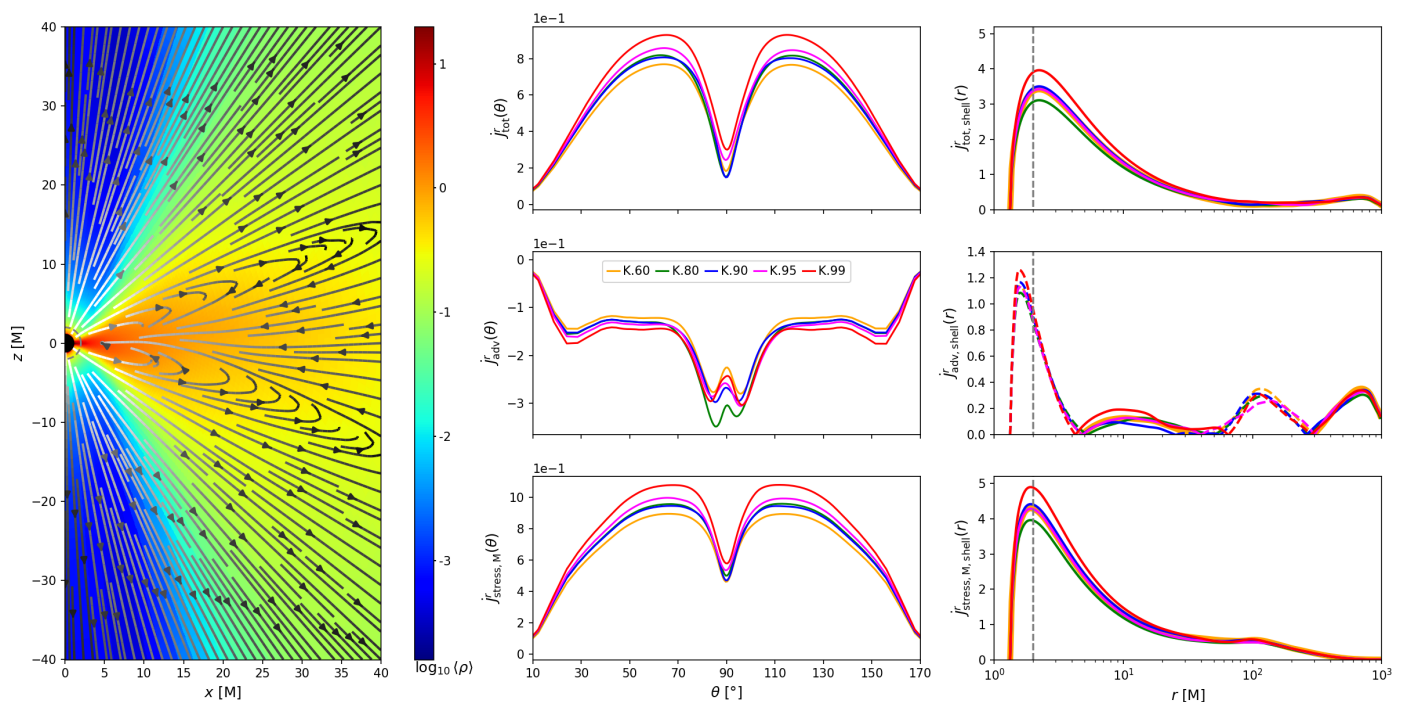


Fig. 6. Left panel: Time and azimuthally averaged density distribution in the meridional plane and total angular momentum flux streamlines (colored by a log-scale of the absolute value; increasing from black to white). Middle column: Polar slices of the radial angular momentum flux at $r = 2 M$, indicated by the dashed, grey lines in the left panel and right column. Shown are total, advective and Maxwell-stress-induced angular momentum fluxes from top to bottom. Right column: Shell-integrated, radial component of the angular momentum fluxes. Solid lines indicate positive values, i.e. outward fluxes and dashed lines are the absolute values of inward (negative) flux.

in a MAD-setup with a high prograde BH spin (cf. (Chatterjee & Narayan 2022) Fig. 10, showing the case of a non-rotating BH in the MAD-setup). The meridional cross-section of the angular momentum vector-field exhibits quite distinct characteristics from the case of the MAD-setup with a non-rotating BH, in that, it exhibits a monopole field-geometry in the jet and wind-region up to a polar angle of $\sim 70^\circ$ and transitioning into a quadrupole field-geometry in the disk and torus. Through this magnetospheric configuration, the polar outflow from jet and wind feeds back into the equatorial inflow in the, opposed to the non-rotating MADs, where there is a transition from an equatorially parallel inflow inside the disk scale height (similar opening angle as the transition to the loops) to the parabolically outflowing angular momentum flux in the jet. The major difference here is the dominance of the angular momentum transport driven by the rotating BH, where the dominantly radial outflow is redirected towards the equatorial plane into the disk, where the torus has to facilitate the radially-outward angular momentum transport in the wind region.

In the middle and right column of Fig. 6, we investigate the impact of the magnetic filling of the MAD-torus on the angular momentum transport. The middle column shows the polar dependence of the time- and azimuthally averaged, radial component of the angular momentum vectors at $r = 2 M$, where there is a maximum in the shell-integrated fluxes. The right panel shows the shell-integrated (see Sec. 2.2 for the definition of shell-integration) and time averaged, radial angular momentum fluxes. The polar slices (indicated by grey dashed lines in the left panel and right column) of J_{tot}^r and $J_{\text{stress,M}}^r$ show a clear model trend. Higher initial magnetic energy from the torus leads to an increase outward angular momentum flux, which is also sustained to larger radii $r \lesssim 50 M$, presented in Appendix Fig. F.1.

In the right panel at the top, one can see that the total shell-integrated fluxes are for one, positive, i.e. radially outgoing flux in the jet and wind are dominant, whereas for the case of a non-rotating BH in Chatterjee & Narayan (2022) Fig. 14, the shell-integrated radial component of the total angular momentum flux is constant and negative up to $r \sim 100 M$. Secondly, the angular momentum fluxes overall peak close to the event horizon of the BH, specifically, inside the ergosphere and drops outside of this region.

We note, that the model-trend is not identical for the shell-integrated total and Maxwell-induced fluxes, since these are affected by the inward advective flux, that is more sensitive to turbulent realisations and does not appear to exhibit any model trend. The model trend is the clearest in the jet sheath opposed to the equatorial plane in both total and Maxwell-induced angular momentum fluxes. Looking at the middle panel, one can clearly see, that the advective, equatorial flux for K.80 is the highest, hence decreasing the total, shell-integrated flux the most for this model. However, we observe that simulation K.99 overall exhibits the highest angular momentum transport both inward, advectively- and predominantly outward, electro-magnetically-driven in jet- and wind-regions. Further we observe, that the model-trend in the jet efficiency and the shell-integrated radial angular momentum fluxes is consistent with one another, which directly links the efficiencies to the angular momentum transport of these simulations.

2.5. Flux Eruptions

We average the data over a time span, in which a MAD-state occurs in each simulation from a subset of three simulations: K.80, K.90 and K.99. In Fig. 7 we emphasize the mass accretion rate and the magnetic flux over the time spans under investigation for

each simulation with a solid line. The time spans of interest in this study were chosen so that the magnetic fluxes through the event horizon have a similar profile, especially for the maximum and minimum amplitudes to be comparable, and the total time span to be $\Delta t = 600$ M. These choices affect the comparability of the different models, especially when interpreting averaged plasma parameters and ray-traced images of azimuthally asymmetric structures, created by the cyclic MAD-states. The notion of better comparability in the indicated time intervals in Fig. 7 are based on the fact that the simulations undergo a very similar increase and decrease in accreted magnetic field, that at the peak of ϕ_{BH} causes the arrestation of the disk. This arises from an advectively driven phase of accumulation of magnetic field in the vicinity of the BH, that then overreaches the threshold magnetic pressure to be accreted and instead outward diffusion of the accreted plasma takes over (Jacquemin-Ide et al. 2025). This is observed to occur in each model at very similar evolution states of the simulations (cf. Fig. 7). The build up of magnetic flux in the beginning of each interval is very similar, as every simulation accretes non-arrested for a very similar time span, as is given for the duration of the arrested states of the disks in all three simulations. The MAD-state (or magnetic flux eruption) is indicated by the decrease in the mass accretion rate (cf. Fig. 7) after both magnetic fluxes and mass accretion rates reach its peak in every simulation. We note, that these time intervals are the only ones within the whole simulations, where we see such strong similarities in the magnetic flux profiles, especially at those similar and importantly late evolution times (~ 17000 M) in the simulations. Since the electromagnetic contribution of the jet power depends quadratically on ϕ_{BH} (Tchekhovskoy et al. (2011)), the EM energy flux contributions to the jet can be ruled out to be a result of strongly differing ϕ_{BH} over the three simulations.

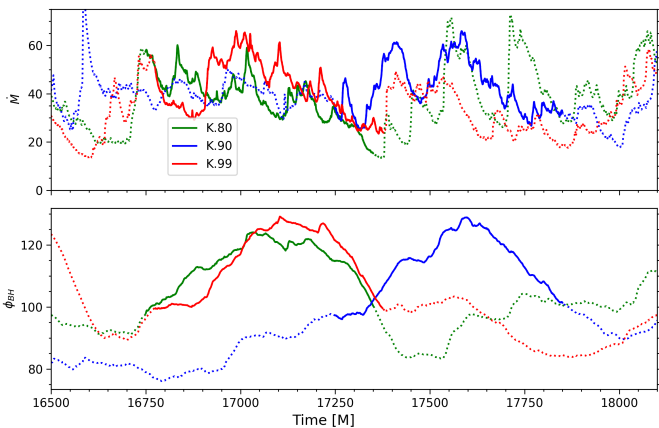


Fig. 7. Interval of investigation in order to compare the jet morphologies of all simulations. The magnetic flux ϕ_{BH} describes a similar curve in height amplitude and width in time intervals for all simulations (indicated by solid lines). The dashed lines solely indicate time intervals that are not of interest for the discussions of the jet morphology.

Simulation	Time interval [M]
K. 80	16750 - 17350
K. 90	17250 - 17850
K. 99	16775 - 17375

Table 2. Time intervals for the respective simulations that are used for most of the GRHMD analysis and completely used for the GRRT (see Fig. 7).

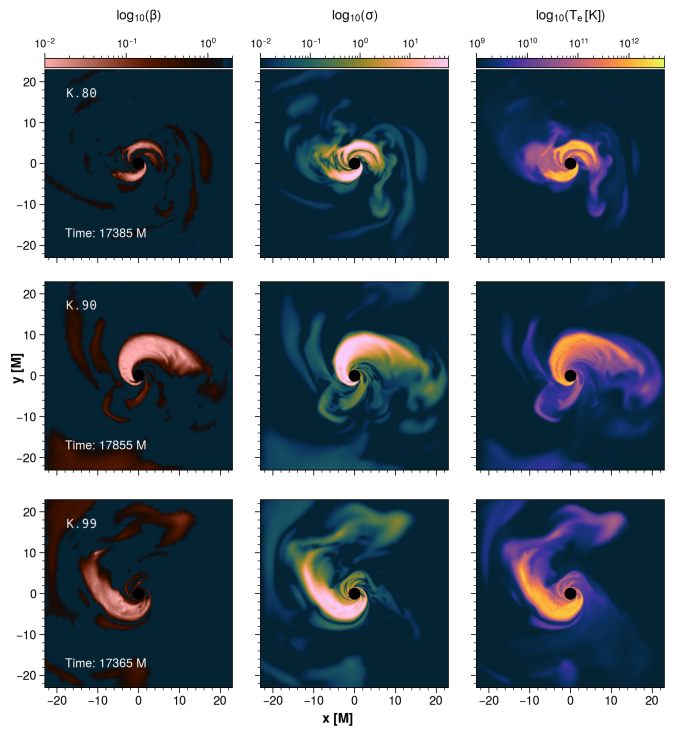


Fig. 8. 2D-slices of the equatorial plane showing plasma- β , σ and T_e of the peak MAD-state of the simulations K. 80, K. 90 and K. 99. Note the extended, arrow-like tail of the flux tube in K. 99 that is twice the length compared to K. 90.

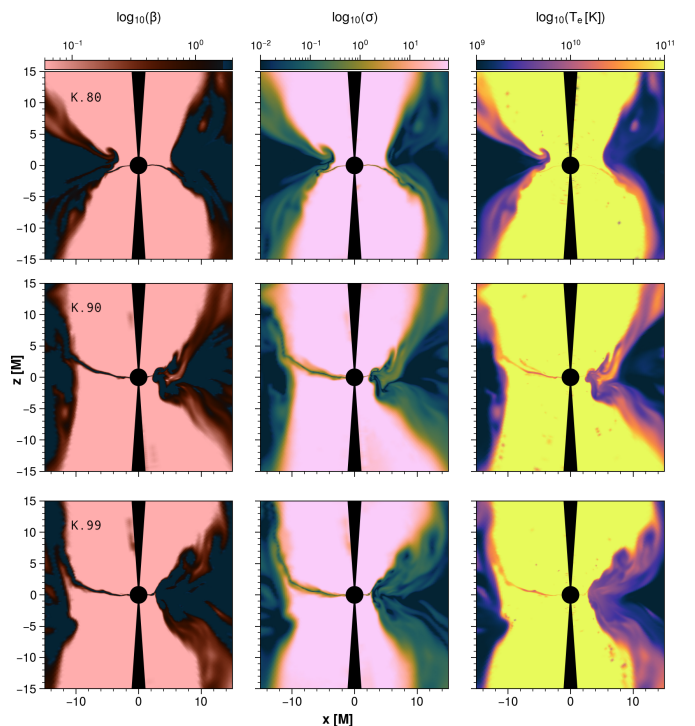


Fig. 9. Meridional 2D-slices of the peak MAD-state showing plasma- β , σ and T_e of the simulations K. 80, K. 90 and K. 99 (equal times as in Fig. 8 for each simulation, respectively). We show the 180° azimuthally rotated cross-section of K. 99, for comparison of the MAD-states.

We want to characterize the magnetic flux eruptions or MAD-states, since their impact on the morphology are imperative to consider in the subsequent analysis. We show respectively si-

multaneous snapshots of the meridional and equatorial planes in the GRMHD simulations, where the flux eruptions are at their respective peak in Fig. 8 and Fig. A.1. We note, that the comparison of the snapshots lie outside the time intervals of comparison Tab. 2, nevertheless the MAD-states impact the simulations inside these intervals already and we show the peak MAD-states to emphasize these effects. We want to demonstrate the maximal impact, that the flux eruptions can have on the plasma parameters and on the radiative signatures. The timescales from the onset of these magnetically arrested states to their peak flux eruptions and finally termination of the arrested disk do not differ significantly across the three models. This in turn aids the comparability of the time-intervals (compare Tab. 2) chosen for time-dependent and -averaged quantities. We want to emphasize that although the amplitude of magnetic flux that is built up and released is very similar across all simulations (cf. Fig. 7) the flux tubes (cf. Porth et al. (2019)) do vary strongly in terms of their electron temperature, magnetization and kinetic to magnetic pressure ratio (see Fig. 8 and Fig. A.1). In the simulation K. 80 these magnetic eruptions occur two-sided in this instance, whereas both K. 90 and K. 99 are completely azimuthally asymmetric (cf. Fig. 8), and the one-sided flux eruptions are much more stable in the latter simulations. K. 99 shows a significantly extended flux tube that is sufficiently hot to imprint clear signatures of thermal synchrotron radiation in the ray-tracings (see Sec. 3 & Fig. G.1). The jet structure is also highly dependent on the MAD-states as these flux tubes are able to contribute to the jet morphology, significantly (see Fig. A.1; K. 99 is again rotated azimuthally by 180°, to compare the MAD-states), and especially introduce high degrees of azimuthal asymmetries, which is important to consider when we investigate time-averaged quantities and morphologies in the following sections.

2.6. Comparison of the Jet Structure

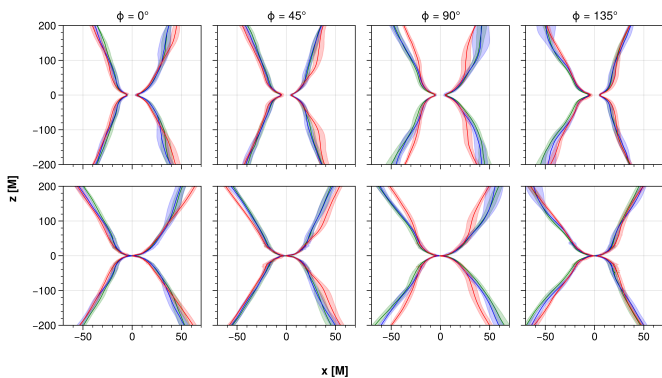


Fig. 10. Upper row: $\sigma = 1$ contours in xz -cross-section corresponding to K. 80 (green lines) K. 90 (blue lines) and K. 99 (red lines) and the 1σ standard deviation in the x -directions over the time intervals listed in Tab. 2. Each column presents poloidal cross-sections at azimuthal angles in 45° increments. Bottom row: Bernoulli parameter $-hu_t = 1.02$ contours, where we otherwise show the exact analogues for it as in the $\sigma = 1$ contours.

We investigate the jet structure and its variability by means of the magnetization σ and the Bernoulli parameter $-hu_t$. The contour at $\sigma = 1 \equiv \sigma_{\text{cut}}$ defines our cut-off of the jet spine in the ray-tracings shown in Sec. 3 and can be interpreted as our inner boundary of the jet sheath. The Bernoulli parameter at $-hu_t > 1.02$ separates the outflowing plasma in the jet from inflowing or gravitationally bound plasma in the disk and wind, so

that we define the $-hu_t = 1.02$ contour as the outer boundary of the jet sheath. In Fig. 10 we show meridional slices (xz -plane) in 45° increments in the azimuthal angle ϕ of the $\sigma_{\text{cut}} = 1$ contour (top row) and the Bernoulli parameter contour at $-hu_t = 1.02$ (bottom row), that are averaged in x -direction over the respective time intervals listed in Tab. 2 for each simulation. Moreover, to emphasize the structural variability we show the standard deviations in x -direction, that are indicated by the colored areas. Note that, by x -directions we denote every axis that is perpendicular to the BH spin vector (in our simulations aligned with the z -axis). We explicitly do not average over ϕ , since the MAD states that are undergone in the chosen time intervals (cf. Fig. 7) introduce strong azimuthal asymmetries that would otherwise smear out.

In Fig. 10, the runs K. 80 and K. 90 trace similar jet boundaries, whereas K. 99 manifests a consistently wider jet for $\phi = \{0^\circ, 45^\circ\}$ and a narrower jet for $\phi = \{90^\circ, 135^\circ\}$. This hints at a rather elliptical paraboloid jet geometry in the K. 99 run, likely induced by the stronger MAD-state that causes the azimuthal axis asymmetry. We note that we have rotated, K. 99 azimuthally by 180° such that the flux eruptions of the simulations match in azimuthal angle. Interestingly, at $\phi = 135^\circ$ all runs consistently show the strongest axis asymmetries, which coincides roughly with the foot point of the flux eruption (compare 8, where the x -Axis is at $\phi = 0^\circ/180^\circ$).

The 1σ -band in Fig. 10 shows consistent structural properties as the Bernoulli contour. The sigma contour is overall significantly narrower downstream the jet and less variable for K. 99, especially at distances $\sim 100\text{M} - 200\text{M}$ from the center, compared to K. 80 and K. 90.

3. General Relativistic Radiative Transfer

In order to investigate the radiative signatures of the 3D GRMHD simulations we calculate the polarized synchrotron emission by means of a general relativistic radiative transfer (GRRT) post-processing step. We therefore employ IPOLE (Mościbrodzka & Gammie (2017)): a semi-analytic code for relativistic polarized radiative transfer.

We assume a model for the electron Distribution Function (eDF), since our GRMHD simulations do neither evolve the electrons simultaneously nor separately, rather they are assumed to tightly follow the evolution of the simulated plasma. The model chosen for this study combines the thermal Maxwell-Jüttner distribution

$$\frac{1}{n_e} \frac{dn_e}{d\Gamma_e} = \frac{\Gamma_e^2 \sqrt{1 - 1/\Gamma_e^2}}{\Theta_e K_2(1/\Theta_e)} \quad (24)$$

and the non-thermal κ -eDF (see Pandya et al. (2016)), that smoothly converges to the Maxwell-Jüttner distribution for low Γ_e

$$\frac{1}{n_e} \frac{dn_e}{d\Gamma_e} = N \Gamma_e \sqrt{\Gamma_e^2 - 1} \left(1 + \frac{\Gamma_e - 1}{\kappa w} \right)^{-(\kappa+1)}, \quad (25)$$

with the normalization factor N , the dimensionless electron temperature $\Theta_e = k_b T_e / m_e c^2$, the modified Bessel-function of the second kind K_2 , the power-law index κ and the width parameter w .

The thermal eDF is the relativistic generalization of the thermal Maxwell distribution and the κ -eDF is inspired by observations of the solar wind and by results of collisionless plasma simulations (e.g. Kunz et al. (2015)) and converges to the thermal

distribution for $\kappa \rightarrow \infty$. Both distributions need an assignment of the electron temperature T_e , which we define as

$$T_e = \frac{pm_p}{R_{p/e} \rho m_e} = \frac{T_{\text{code}} m_p}{R_{p/e} m_e}, \quad (26)$$

where k_B , m_p and m_e are respectively the Boltzmann constant and the proton and electron masses. ρ and p are the rest-mass density and pressure from the GRMHD simulation, respectively. The code temperature $T_{\text{code}} = p/\rho$ is thus defined by plasma parameters from the GRMHD code as well and describes solely the ion temperature in code units. The ratio of proton temperature T_p and electron temperature T_e , R , is defined as

$$R_{p/e} = \frac{T_p}{T_e} \equiv R_{\text{high}} \frac{\beta^2}{\beta^2 + 1} + R_{\text{low}} \frac{1}{\beta^2 + 1}, \quad (27)$$

with the plasma parameter $\beta = 2 \frac{p}{b^2}$ provided by the simulation. The so called R- β model then has two parameters in total, R_{high} and R_{low} (see Mościbrodzka et al. (2016)), that together with the code temperature control the electron temperature. Notice, that we have to assert an electron temperature model as the GRMHD simulation does not intrinsically provide an electron temperature.

The kappa distribution in Eq. (25) is defined by its width, w , which is now attributed a fraction ε of the magnetic energy besides the thermal energy (see Davelaar, Jordy et al. (2019) and Fromm et al. (2022)):

$$w := \frac{\kappa - 3}{\kappa} \Theta_e + \frac{\varepsilon}{2} \left[1 + \tanh(r - r_{\text{inj}}) \right] \frac{\kappa - 3}{6\kappa} \frac{m_p}{m_e} \sigma. \quad (28)$$

The injection radius, r_{inj} , is the distance from the BH, where electrons with magnetic energy contribution are injected and $\sigma = b^2/\rho$.

The non-thermal contributions to the electron energies are thought to be originated in magnetic reconnection events, in which current sheets accelerate the charged particles. These processes cannot be resolved in global GRMHD simulations, therefore, the κ -parameter depends on the magnetization and plasma- β when employing a PIC simulation based sub-grid model from Ball et al. (2018):

$$\kappa := 2.8 + 0.7\sigma^{-1/2} + 3.7\sigma^{-0.19} \tanh(23.4\sigma^{0.26}\beta) \quad (29)$$

With that we again follow Fromm et al. (2022) and Davelaar, Jordy et al. (2019) (In the former study, a more detailed parameter space study on the R- β model can be found).

3.1. M87 Ray-Tracing Setup

For the 86 GHz Ray-Tracings, we fixed the parameters of all runs to the mass of the BH of $M_{\text{BH}} = 6.2 \times 10^9 M_{\odot}$ (cf. Gebhardt et al. 2011; EHT Collaboration et al. 2019a,b,c), the distance to the BH to $D = 16.9$ Mpc (cf. Blakeslee et al. 2009; Cantiello et al. 2018; EHT Collaboration et al. 2019b,c) and the viewing angle $i = 163^\circ$ (as spanned by the BH spin axis and line of sight) of the BH and jet in M87. The parameters for the electron temperature model are set to $R_{\text{high}} = 160$ and $R_{\text{low}} = 1$ and for the κ -eDF in Eq. (25), we choose a non-thermal emission fraction of $\varepsilon = 0.5$ and a injection radius of non-thermal particles at $r_{\text{inj}} = 10$ M. We note that the numerical approximations of the emission and absorption coefficients are only valid in the range $3.1 \geq \kappa \leq 8$, where solely the κ -eDF is applied, and the Maxwell-Jüttner eDF

otherwise.

This means that we mainly calculate non-thermal emission in the the jet-sheath and it is noted that the Flux-tubes can also be sufficiently magnetized, such that they emit non-thermally.

A polar cut of $\theta_{\text{cut}} = 4^\circ$ (opening angle of the cut-out cone is $\alpha_{\text{cone}} = 8^\circ$) is applied for the ray-tracings as shown before in the GRMHD data (cf. Appendix B Fig. B.1 and Fig. A.1). Additionally, we omit the emission from the jet-spine in all regions where $\sigma > \sigma_{\text{cut}} = 1$. This is due to the fact that the highly dominant magnetic energy in the jet-spine is prone to introduce small errors in the total energy evolution, drastically altering the internal energy, hence the plasma temperature.

The time-averaged flux of each ray-traced simulation is adjusted such that the flux at horizon scale at 230 GHz matches the observed 0.9 Jy by the EHT Collaboration et al. (2019a) by means of optimizing the mass-accretion rates in the GRMHD simulations.

3.2. Comparing Jet Structure and Polarization at 86 GHz

In Fig. 11 we present polarized, time-averaged ray-tracings of the three simulations up to the 0.5 mas-scale, averaged over the time-intervals as used before (cf. Tab. 2). These images are the result of a line-integral convolution (LIC) of the electric vector position angle (EVPA) with a field of random generated numbers. This generates stream lines of the EVPA vector field, encoding directional information of the field lines. The intensity I is then super-imposed onto the LIC of the EVPAs, where the opacity of those is a function of the linear polarization (LP) fraction. The image is then rescaled so that the maximum of the convolved image $\max[f(I, m, \text{EVPA}_{\text{field-lines}})]$ equals $\max(I)$. The LP fraction is given by:

$$m = \frac{\sqrt{Q^2 + U^2}}{I} \times 100 [\%] \quad (30)$$

Qualitatively, one can tell by the dominance of the stream lines over the smooth Stokes- I in Fig. 11, that K. 99 exhibits the highest linear polarization of all runs. Quantitatively, we show the LP fraction and I in Fig. 12 as a function of time, offset by a time T_i , such that the time-intervals in Tab. 2 have a common starting time for comparison purposes. The LP fraction peaks at $\sim 16\%$ for K. 99 compared to $\sim 11\%$ in the normal accretion states for both K. 80 and K. 90. The LP-pattern itself of K. 99 differs as well, in that the EVPA longitudinal component (to the jet position angle) inside the jet is clearly dominant, as can be seen by the straight lines over a wide area inside the jet. Comparing this observation to K. 80 and K. 90, those on the other hand, exhibit visible transverse components in most parts of the EVPAs. At the jet edge, this behaves analogously for K. 99, where the EVPAs now sharply transition from following the jet longitudinally in the inside to a dominant EVPA-field perpendicular to the jet edge. This hints at a highly ordered magnetic field in the jet spine.

Notably, the jet structure of K. 99 is very distinct from the usual paraboloidal shape that is associated with MAD-simulations. Beyond the jet base, about $\sim 30 \mu\text{as}$ from the core, the jet transitions into a cone-like shape, which will be discussed in more detail in the next section.

3.3. Jet Edge and Width Profiles

In Fig. 13, we trace the profile of the jet analogously to the structural investigation of the jet sheath in section 2.6. We

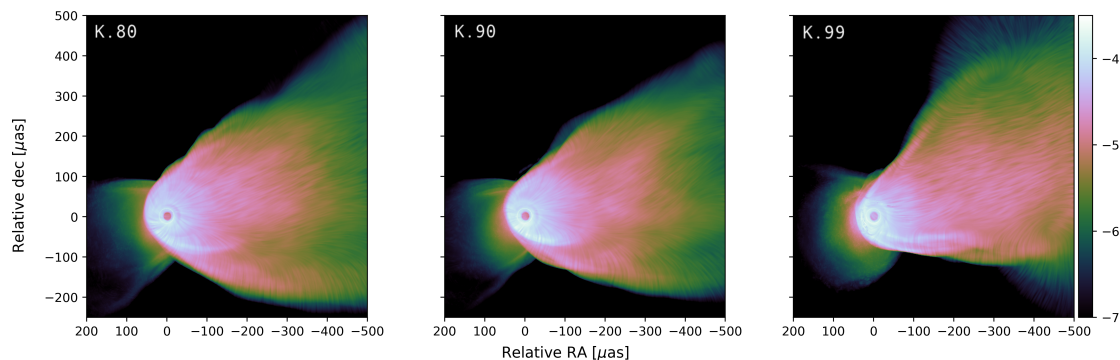


Fig. 11. Time-averaged 86 GHz ray-tracings of the M87 jet. Each simulation is averaged over the time intervals corresponding to each simulation that are listed in Tab. 2. Stokes-I is super-imposed with a line integral convolution of the EVPA vector field by scaling the opacity as a function of the linear polarization fraction and rescaling the image by rescaling the maximum of the convolved image $\max[f(I, m, \text{EVPA}_{\text{vector-field}})]$ to $\max(I)$.

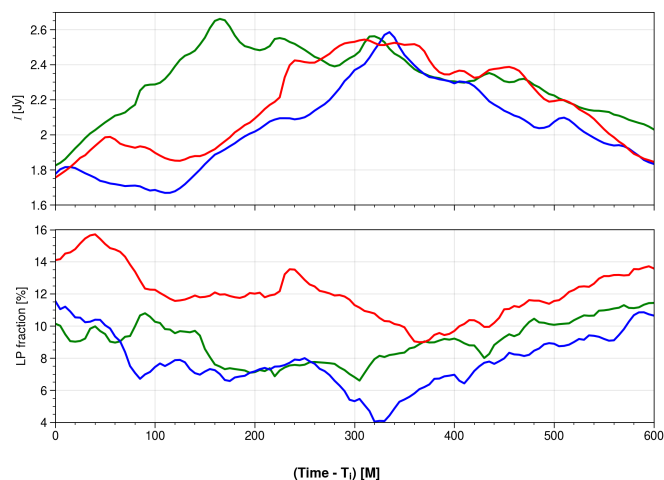


Fig. 12. Top row: 86 GHz light curve for simulations K. 80 (green) K. 90 (blue) and K. 99 (red) in the time intervals shown in Tab. 2 but shifted by an offset for reasons of better comparability. Bottom row: Linear Polarization fraction with the same color-code as before.

extract the time-averaged contours at $\langle I \rangle = 5 \times 10^{-6}$ Jy (solid lines) and illustrate with the corresponding colored areas the variability perpendicular to the jet position angle (PA), i.e. the 1σ -bands of the variation in jet-PA-perpendicular direction of the $I = 5 \times 10^{-6}$ Jy contour over time. Therefore, the images were de-rotated to a jet PA of -180° (South-North direction) such that the jet can be subdivided into jet PA perpendicular slices for each pixel along the jet direction. The closest pixel to the contour is determined at each time step. Eventually, the mean and standard deviation at each slice over time can be calculated. The chosen contour of $I = 5 \times 10^{-6}$ Jy is a sensible tracer of something that could be considered the edge of the jet, which is in itself loosely defined, since it traces the apparent jet edge visible from Fig. 11 at a dynamic range of about four orders of magnitude. In observations of the jet of M87* often the observed edge-brightening is the best indicator of the jet edge (often taken to be the HWHM towards the outside of the jet of the bright Gaussian edge features). In these simulations on most scales the jet perpendicular flux-profile does not exhibit bi- or multimodal distributions, especially not time-averaged, such that bright spots are not as pronounced on the edge of the jet. The mean contours of K. 80 and K. 90 are very similar, whereas K. 99 stands out by its partially cone-like shape as pointed out in

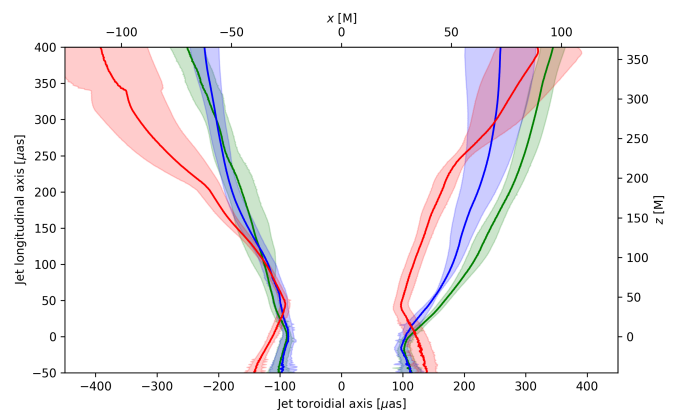


Fig. 13. $\langle I \rangle = 5 \times 10^{-6}$ [Jy] contours of the time averaged 86 GHz ray-tracings (not the line integral convolved images) shown in Fig. 11 for simulations K. 80 (green) K. 90 (blue) and K. 99 (red). The colored areas are 1σ -bands of the standard deviations in the toroidal direction.

the last section. The actual difference in the asymmetries of the models becomes very apparent. In a basis defined by coordinates (x, z) as in Fig. 13, we find that the asymmetry is strongly shifted to negative x -values in K. 99. The variability of the jet structure provides confidence that the jet structures shown in Fig. 11 are not distorted because of strong time-dependent morphological variations. The variation of these contours in x -direction slowly increase in z -direction in the cases of K. 80 and K. 90, but increase rather abruptly and asymmetrically for K. 99 on the positive x half-space at ~ 250 M and on the negative one at ~ 200 M. This can be explained by a helical arc propagating through the jet sheath, seen in Fig. 11 downstream the jet in K. 99. Nevertheless, the jet shape of K. 99 is completely altered in comparison to K. 80 and K. 90.

From these jet profiles of the 86 GHz ray-tracing we can now extract the jet widths as a function $W(z)$ of the jet longitudinal axis z (as defined before) and compare these to the observations of Lu et al. (2023) shown in Fig. 14. We note that the data-points of the jet-width measurements do not show the error-bars in Lu et al. (2023), hence we cannot elaborate on the statistical certainty of this comparison. From Fig. 14, it is apparent that the theoretical predictions especially of K. 80 and K. 90 do match the observations well at the scales below $100 \mu\text{as}$, contrarily to

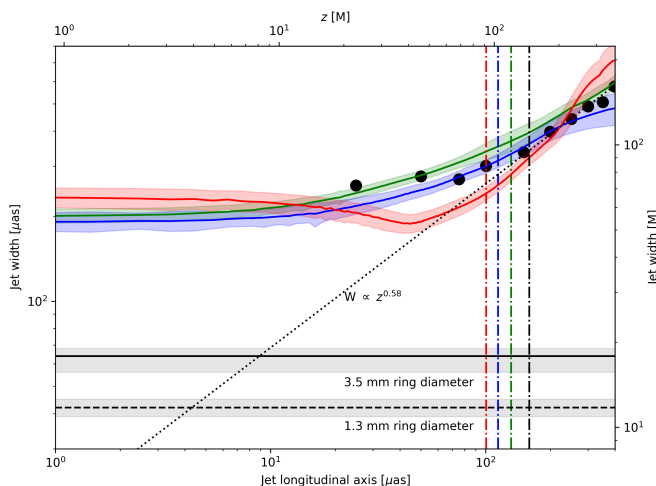


Fig. 14. Jet width of M87 at 86 GHz along the longitudinal jet axis for simulations K. 80 (green) K. 90 (blue) and K. 99 (red) with corresponding 1σ -bands. The black dots are data points of the jet width of M87 from the observation of Lu et al. (2023). The dotted line is a power-law fit from observations of M87 (source). The solid horizontal line is the estimated 86 GHz ring size and the dashed horizontal line is the 230 GHz ring size with respective error band (gray areas). The vertical lines are the distances from the BH, where the intrinsic half-opening angles equals the jet viewing angle of $\theta_v = 17^\circ$ (color-code is consistent).

the claims of Lu et al. (2023) that MAD simulations may have difficulty explaining the observed jet width at these scales. At the scales shown above $100 \mu\text{as}$ the simulations K. 80 and K. 90 converge to the extrapolated $W(z) \propto z^{0.58}$ power law fit from large scale observations (see Asada & Nakamura (2012), Hada et al. (2013), Hada et al. (2016)). K. 99 follows the power-law further up-stream and exhibits a sudden increase of the jet width at $\sim 40 \mu\text{as}$, whilst even closer to the BH it becomes almost constant, but even wider than the other models. This sudden increase in the width of the jet can be explained by the counter-jet, which exhibits a wider opening angle and thus shifts the jet edge of the counter-jet to positive z -values up to $\sim 100 \text{ M}$ (cf. Fig. 11, right image). For the common choice of the R- β electron temperature- and κ non-thermal electron prescriptions chosen here K. 99 exhibits a steeper slope than this observation suggests, rather following the large-scale power-law. The new observational data points at the scales closer to the jet launching region suggest that K. 90 satisfies these observations very well, as the data points are very well within the variability of K. 90 (cf. green band in Fig. 14). We also see that this holds mostly for the common model K. 80, as well.

3.4. Ray-Tracing the Flux Eruptions

Since we mostly study the time-averaged quantities of the simulations presented in this work to extract general physical differences from the three models, we have to also shed light on the influence of the episodic magnetic flux eruptions on the radiative signatures (cf. in Sec. 2.5 we discussed the consequences of the flux eruptions on the GRMHD quantities). In Fig. G.1 we show an example of a ray-tracing of such a flux eruption in the case of model K. 99, where on the left we only ray-traced the disk emission and on the right the full emission that includes emission from the jet, as well. By comparison of both images, the influence of the flux eruption on the jet morphology becomes clear. The jet base strongly deviates from a paraboloid as the flux erup-

tion envelopes the jet in an azimuthally asymmetric manner (cf. the feature in the upper half of the right image in Fig. G.1). Since these flux eruptions are intermittent phenomena, they do not influence the radiative imprints on the jet morphology steadily and azimuthally symmetric, and are thus important to consider for the study of the long time-scale structural studies of MAD simulations. In order to be able to average out the strong azimuthal asymmetries introduced by MAD states, they have to be averaged over multiple ones. Since they occur quasi-periodically with a frequency of the order of $\sim 1000 \text{ M}$, this would make studies on time-scales of at least 10000 M necessary. Hence, we limited our discussion to one MAD event per simulation.

4. Conclusions

We find that the initial magnetic energy content of the torus systematically alters the jet energetics and morphology of the developed simulations. It affects mostly the EM contribution in the Jet and from that gains $\sim 60\%$ efficiency in the conversion from rest-mass energy to the energy of the outflow by means of increasing the magnetic energy of the torus, at the initialization. This in turn, can make nonthermal particle acceleration from vacuum gaps and subsequent pair cascades more likely, due to the increased EM-field in the jet spine (cf. Levinson & Rieger 2011; Wendel et al. 2021, for details on the vacuum gap model and applications to low-luminosity AGN like M87 and Mrk501). We also find, that an increased magnetic filling of the FM torus elevates the outward angular momentum transport, primarily in the jet, driven by Maxwell-stresses. Comparing the angular momentum transport of BHs with very high spin presented here to Chatterjee & Narayan (2022), in which the case of a non-rotating BH in a standard MAD-setup ($F = 0.8$) is investigated, the major differences are: *i*) the total radial angular momentum flux is dominated by radially outward directed flux in the jet and wind, majorly originating from the jet base. *ii*) Morphologically, the angular momentum vector-fields are distinct, in that the high spin BH creates field-lines that point radially outwards in a polar angle range from $\sim (0 - 70)^\circ$ or $\sim (110 - 180)^\circ$. Towards the equatorial plane the field-lines transition from a monopole-geometry to a quadrupole-geometry in the disk and torus. The dominant, Maxwell-stress induced, outward polar flux is redirected to an equatorially inward, advectively driven flux. In contrast, the case of a non-rotating BH exhibits dominant advectively driven inward angular momentum flux in a larger portion of the disk and torus, whereas the outward directed Maxwell-stress induced flux is subdominant in the jet, such that the net angular momentum is transferred to the central BH. The outward angular momentum transport also covers a much smaller polar angle compared to simulations with high spin, contributing far less to the strength of outward winds. Our simulations demonstrate the effect of extracting the angular momentum of the BH to the angular momentum of the outflowing plasma in the jet and wind as proposed by (Blandford & Znajek 1977) for the first time in MADs with high spin BHs. We further find that there is a maximum of all net angular momentum fluxes inside the ergospheric region of the BH, opposed to the net-constant fluxes for MAD-simulations with no spin.

It appears that the disk-vertical flux tubes created by the magnetically arrested disk affect the jet structure more pronounced for high filling factors. From our sampled MAD states, we find a tendency for spatially more extended flux tubes that affect the jet morphology by introducing significant azimuthal asymmetries in the case of K. 99 that propagate along the jet at least up to 200 M . The jet sheath structure is more stable on these scales, i.e. the jet structure exhibits lower variability in the jet-perpendicular direction. However, since we restricted the jet morphology analysis to a time-interval, in that a single flux eruption occurs in each simulation, further detailed, statistical

analysis of the impact of the filling factor on the quasi-periodic flux eruptions could provide valuable insights into the observable footprints that they have.

The radiative transport calculations as well show that the jet-sheath structure is more stable and collimated up to $\sim 200 \mu\text{as}$ supported by the higher EM energy flux contribution in K. 99. We find significantly elevated LP fractions up to $\sim 15\%$ in agreement with observations of the [EHT Collaboration et al. \(2021b\)](#). The jet width relation over the jet axial distance shows that GRRT calculations of GRMHD simulations of magnetically arrested accretion flow is able to match the observed jet width profile of [Lu et al. \(2023\)](#) very well for the reference models. For K. 99 we find deviations from the jet width, as it follows the observed large-scale power-law relation $W \propto z^{0.58}$ to shorter distances, whereas the observations follow a sub-power-law relation. The deviation of K. 99 from the observations, however, is a result of the different techniques used for the determination of the jet width. In the observations of [Lu et al. \(2023\)](#) the HWHM of the outermost components perpendicular to the jet longitudinal axis determines the jet width, whereas we do not recreate the edge brightened jet morphology and thus use brightness contours to determine the jet width. This makes the detailed jet width relation difficult to compare to these observations, nevertheless we show that all our MAD simulations provide a wide jet base, substantially wider than the pure Blandford-Znajek (BZ) jet (cf. [Blandford & Znajek 1977](#)) for a high spin BH ($a \rightarrow 1$). This is evident from our analysis of the jet energy fluxes, that the almost evacuated, highly magnetized jet spine ($\sigma \gtrsim 1$) is dominated by EM energy flux and in the enveloping jet sheath the wind contributes to the outflowing kinetic energy flux increasing with distance. This jet sheath region ($\sigma \lesssim 1$ and the gravitationally unbound part of the plasma) is the origin of the jet emission and the $\sigma = 1$ contour, hence, is not a good tracer for the outermost jet edge that could be observed. We remind here, that $\sigma = \sigma_{\text{cut}} = 1$ is the value for the emission cut-off for the jet spine, where we do not expect significant synchrotron emission in the radio-regime because of the extremely low electron densities, as well as efficient synchrotron cooling, due to the presence of high magnetic field strengths in $\sigma \gg 1$ regimes. We stress that a simple extrapolation and comparison of plasma parameters such as the magnetization from simulations to trace the edge or width of the jet observed at mm-wavelengths (cf. [Lu et al. 2023](#), Fig. 3: grey band shows σ -contours from force-free electrodynamic simulations of a BZ jet for different BH spins) is insufficient to approximate the complex emission processes, that are yet to be fully understood. From the GRRT of our GRMHD simulations for the jet of M87* it is evident that the apparent width of the jet base is not anchored at the ergosphere of the BH, opposed to force-free electrodynamic simulations.

Overall we find the jet of the K.99-model to exhibit more flux downstream the jet compared to the reference models. This aids in solving the issue that GRMHD simulations produce jets that decline too much in flux downstream compared to observations. Hence, this model is well suited for modelling jets on larger scales, beyond the jet launching region. This is very helpful, since most SMBH-systems in the universe are of smaller angular-size to us than M87*. With the enhanced jet power in this model, the jet remains brighter and more collimated on scales even beyond 1000 M.

The magnetic filling factor regulates the spatial extent of the initial vector potential and thus that of the magnetic field, as well as the total magnetic energy inside the initial torus configuration of our simulations, that are commonly used to model magnetically arrested accretion and also constitutes the main portion of the simulation library used for M87 by the [EHT Collaboration et al.](#) In general, we conclude from this

study that the evolution of these MAD simulations is very sensitive to minor changes in the initial magnetic field in the FM torus, set by the filling factor. In order to keep track of the vast parameter space of MAD simulations and consequences of the initial conditions, the specification of the detailed, initial vector-potential of simulations is therefore paramount.

Acknowledgements. We thank Charles F. Gammie for the helpful discussion regarding this work. This research is supported by the DFG research grant ‘‘Jet physics on horizon scales and beyond’’ (Grant No. 443220636) within the DFG research unit ‘‘Relativistic Jets in Active Galaxies’’ (FOR 5195). The numerical simulations and calculations have been performed on MISTRAL at the Chair of Astronomy at the JMU Wuerzburg. YM is supported by the National Key R&D Program of China (grant no. 2023YFE0101200), the National Natural Science Foundation of China (grant no. 12273022), and the Shanghai municipality orientation program of basic research for international scientists (grant no. 22JC1410600)

References

- Acciari, V. A., Ansoldi, S., Antonelli, L. A., et al. 2020, *MNRAS*, **492**, 5354–5365
- Antón, L., Zanotti, O., Miralles, J. A., et al. 2006, *ApJ*, **637**, 296
- Asada, K. & Nakamura, M. 2012, *ApJ*, **745**, L28
- Ball, D., Sironi, L., & Özel, F. 2018, *ApJ*, **862**, 80
- Blakeslee, J. P., Jordán, A., Mei, S., et al. 2009, *ApJ*, **694**, 556
- Blandford, R. D. & Znajek, R. L. 1977, *MNRAS*, **179**, 433
- Cantiello, M., Blakeslee, J. P., Ferrarese, L., et al. 2018, *ApJ*, **856**, 126
- Chatterjee, K. & Narayan, R. 2022, *ApJ*, **941**, 30
- Cho, H. & Narayan, R. 2025, Variability in Black Hole Accretion: Dependence on Rotational and Magnetic Energy Balance
- Cruz-Orsorio, A., Fromm, C. M., Mizuno, Y., et al. 2022, *Nature Astronomy*, **6**, 103
- Davelaar, Jordy, Olivares, Hector, Porth, Oliver, et al. 2019, *A&A*, **632**, A2
- EHT Collaboration, Akiyama, K., Alberdi, A., et al. 2023, *ApJ*, **957**, L20
- EHT Collaboration, Akiyama, K., Alberdi, A., et al. 2019a, *ApJ*, **875**, L1
- EHT Collaboration, Akiyama, K., Alberdi, A., et al. 2021a, *ApJ*, **910**, L12
- EHT Collaboration, Akiyama, K., Alberdi, A., et al. 2019b, *ApJ*, **875**, L6
- EHT Collaboration, Akiyama, K., Alberdi, A., et al. 2019c, *ApJ*, **875**, L5
- EHT Collaboration, Akiyama, K., Algaba, J. C., et al. 2021b, *ApJ*, **910**, L13
- Fishbone, L. G. & Moncrief, V. 1976, *ApJ*, **207**, 962
- Fromm, C., Cruz-Orsorio, A., Mizuno, Y., et al. 2022, *A&A*, **660**
- Gebhardt, K., Adams, J., Richstone, D., et al. 2011, *ApJ*, **729**, 119
- Hada, K., Kino, M., Doi, A., et al. 2016, *ApJ*, **817**, 131
- Hada, K., Kino, M., Doi, A., et al. 2013, *ApJ*, **775**, 70
- Jacquemin-Idé, J., Begelman, M. C., Lowell, B., et al. 2025, Demystifying flux eruptions: Magnetic flux transport in magnetically arrested disks
- Kim, J.-S., Mueller, H., Nikonov, A. S., et al. 2024a, Imaging the black hole shadow and extended jet of M87
- Kim, J.-S., Nikonov, A. S., Roth, J., et al. 2024b, *Astronomy & Astrophysics*, **690**, A129
- Kim, J.-Y., Krichbaum, T. P., Lu, R.-S., et al. 2018, *A&A*, **616**, A188
- Kunz, M. W., Schekochihin, A. A., Chen, C. H. K., Abel, I. G., & Cowley, S. C. 2015, *Journal of Plasma Physics*, **81**, 325810501
- Lalagos, A., Tchekhovskoy, A., Most, E. R., et al. 2025
- Levinson, A. & Rieger, F. 2011, *ApJ*, **730**, 123
- Lu, R.-S., Asada, K., Krichbaum, T. P., et al. 2023, *Nature*, **616**, 686–690
- Mizuno, Y. & Rezzolla, L. 2024, General-Relativistic Magnetohydrodynamic Equations: the bare essential
- Mościbrodzka, M., Falcke, H., & Shiokawa, H. 2016, *A&A*, **586**, A38
- Mościbrodzka, M. & Gammie, C. F. 2017, ipole - semianalytic scheme for relativistic polarized radiative transport
- Noble, S. C., Krolik, J. H., & Hawley, J. F. 2010, *ApJ*, **711**, 959
- Olivares, H., Porth, O., Davelaar, J., et al. 2019, *A&A*, **629**, A61
- Pandya, A., Zhang, Z., Chandra, M., & Gammie, C. F. 2016, *ApJ*, **822**, 34
- Porth, O., Chatterjee, K., Narayan, R., et al. 2019, *ApJ Supplement Series*, **243**, 26
- Prather, B. S. 2024, KHARMA: Flexible, Portable Performance for GRMHD
- Prather, B. S., Wong, G. N., Dhruv, V., et al. 2021, *Journal of Open Source Software*, **6**, 3336
- Sano, T., Inutsuka, S.-i., Turner, N. J., & Stone, J. M. 2004, *ApJ*, **605**, 321
- Schmitt, J. H. M. M. & Reid, M. J. 1985, *ApJ*, **289**, 120
- Snios, B., Nulsen, P. E. J., Kraft, R. P., et al. 2019, *ApJ*, **879**, 8
- Takahashi, R. 2008, *MNRAS*, **383**, 1155
- Tchekhovskoy, A., Narayan, R., & McKinney, J. C. 2011, *MNRAS*, **418**, L79
- Wendel, C., Shukla, A., & Mannheim, K. 2021, *The Astrophysical Journal*, **917**, 32
- Yang, H., Yuan, F., Li, H., et al. 2024, *Science Advances*, **10**, 3544

Appendix A: Initial Magnetic Field Configuration and Filling-scaling of the Tori

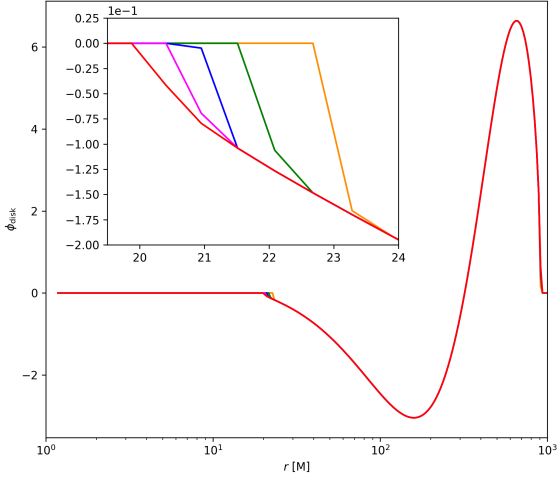


Fig. A.1. Initial disk-vertical magnetic flux permeating the disk. The colors correspond to simulations K. 60 (orange), K. 80 (green), K. 90 (blue), K. 95 (magenta) and K. 99 (red).

Here, we calculate the initial covariant volume fractions of the volume containing the cells in which the initial invariant magnetic field strength b is defined and the initial volume enclosing the full mass density distribution of the torus. The initial magnetic field is normalized such that the minimum of plasma- β in the torus is $\beta_{\text{min}} = 100$ in all simulations. We calculate the total and shell-integrated covariant volumes of the torus and enclosed magnetic field as follows:

$$V_t = \int_{\{\rho > 8 \times 10^{-7}\}} \sqrt{-g} dr d\theta d\phi, \quad V_b = \int_{\{b > 1 \times 10^{-7}\}} \sqrt{-g} dr d\theta d\phi, \quad (\text{A.1})$$

$$V_t(r) = \int_{\{\rho > 8 \times 10^{-7}\}} \sqrt{-g} d\theta d\phi, \quad V_b(r) = \int_{\{b > 1 \times 10^{-7}\}} \sqrt{-g} d\theta d\phi, \quad (\text{A.2})$$

We choose the masking conditions for the enclosed volume of the density distribution such that ρ is above the density distribution in the atmosphere (the space excluding the torus and BH), that should have its minimum at $\rho_{\text{min}} = 10^{-6}$ (as stated in Sec. 2), however, increases up to $\rho \sim 8 \times 10^{-7}$ in the vicinity of the BH. For b , the condition is not as strict, since its numeric value is only defined, where the four-vector potential A_ϕ contributes to the curl to generate the magnetic field. We choose a low threshold of $b > 1 \times 10^{-7}$ and set the non-defined values that are mostly outside the torus to 0 in order to capture the full volume of the initial magnetic field. The actual filling factor is then given by:

$$f_a = \frac{V_b}{V_t}, \quad f_a(r) = \frac{V_b(r)}{V_{\text{torus}}(r)}. \quad (\text{A.3})$$

We note that, f_a is a measure for the *actual* volumetric magnetic field extent (volumetric filling forth on), or the *magnetic filling* of the initial magnetospheric configuration, that we calculate for each filling factor F and is not equivalent to the latter values as can be seen in Tab. A.1. The total volumina contained by magnetic fields is generally quite close to the constant torus volumes throughout the simulations (cf. Fig. ??), much closer than the filling factors F suggest. However F , simply scales the offset of the initial vector potential A_ϕ cf. Eq. (6), essentially increasing its offset from the zero cut-off maximum function in Eq. (6) as can also be seen in Fig. 1. Still, increasing F indeed leads to an increased volume that contains magnetic fields. Hence, we use the filling

Table A.1. Initial volume percentage of the torus filled by magnetic fields f_a compared to the initial parameters F , the filling factors, for each simulation.

Simulation	K. 60	K. 80	K. 90	K. 95	K. 99
F	0.60	0.80	0.90	0.95	0.99
f_a [%]	99.16	102.06	103.57	104.41	105.62

factor synonymously with the scaling of the magnetic field extent and the magnetic energy in the FM-torus.

Appendix B: Average MHD Parameters

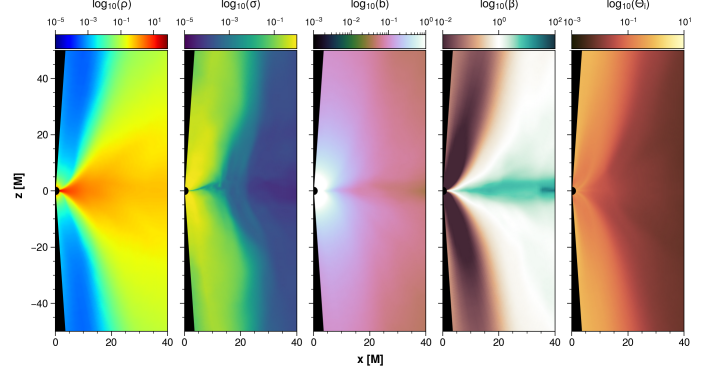


Fig. B.1. Time and azimuthally averaged plasma (MHD) parameters of model K.99. The time is averaged over the interval indicated in Fig. 7 and listed in Tab. 2. We apply a polar cut of $\theta_{\text{cut}} = 4^\circ$ in the post-processed ray tracings for all models, which is indicated by the black regions at the poles.

Appendix C: Mass-Accretion Rate

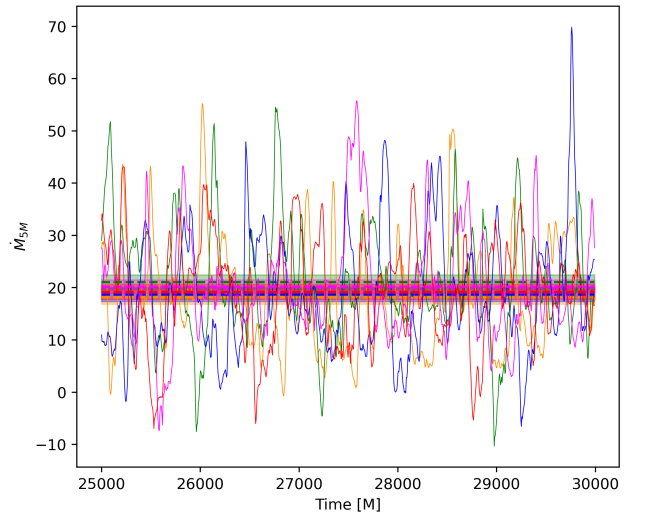


Fig. C.1. Mass-accretion rate \dot{M}_{5M} of simulations K. 60 (orange), K. 80 (green), K. 90 (blue), K. 95 (magenta) and K. 99 (red). The horizontal lines are the averages and the shaded area span the $2\sigma_{\text{corr}}$ confidence interval of the correlated time series. The overlapping error-bands show that the mass-accretion rate is sufficiently similar in between all simulations, thus, indicating that these are in a steady-state.

Appendix D: MRI Quality Factors

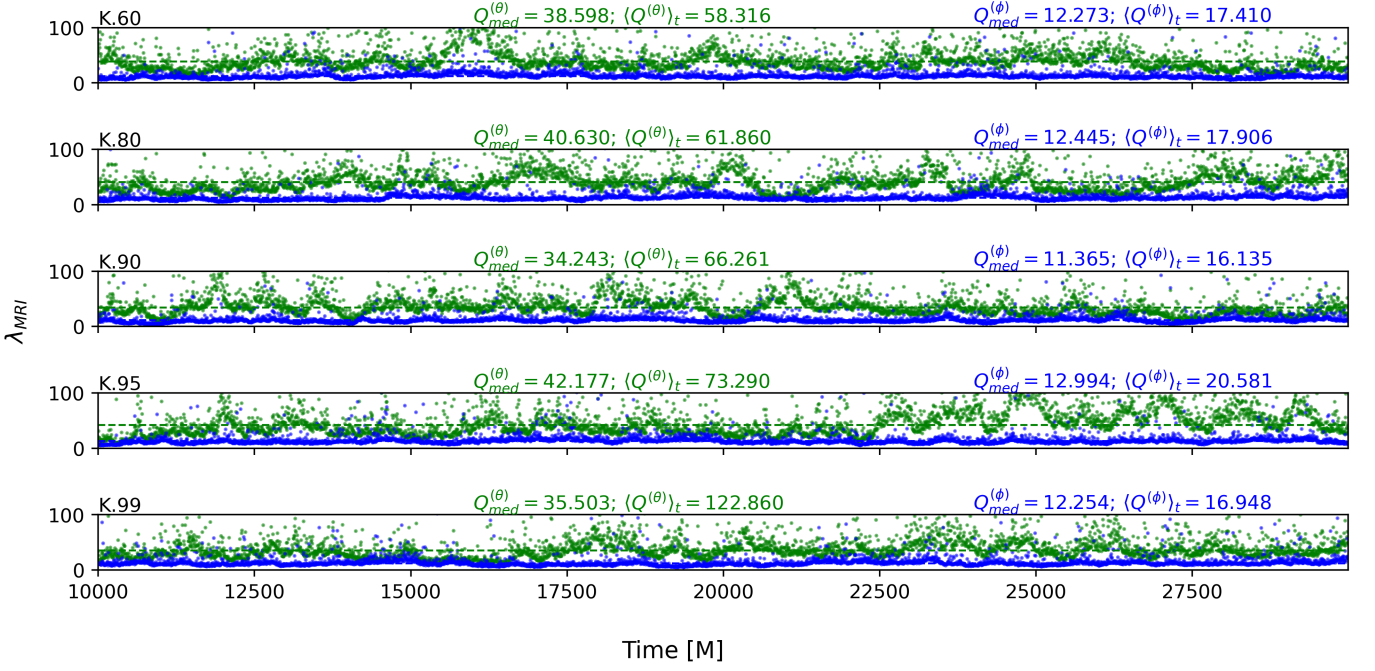


Fig. D.1. Disk averaged MRI quality factors in θ and ϕ of each simulation, rowwise. Dashed lines are the median values taken over the time span shown in the graphs. Besides the median values we also give corresponding time averaged values. Due to the skewed nature of the temporal distribution of the disk averaged Q-factors, the median is more appropriate for interpretation. It is noted that for $Q^{(\theta)} \sim (3-6)\%$ of points lie outside the graph, i.e. are above 100 in the three simulations. For $Q^{(\phi)} \sim 1\%$ are concerned.

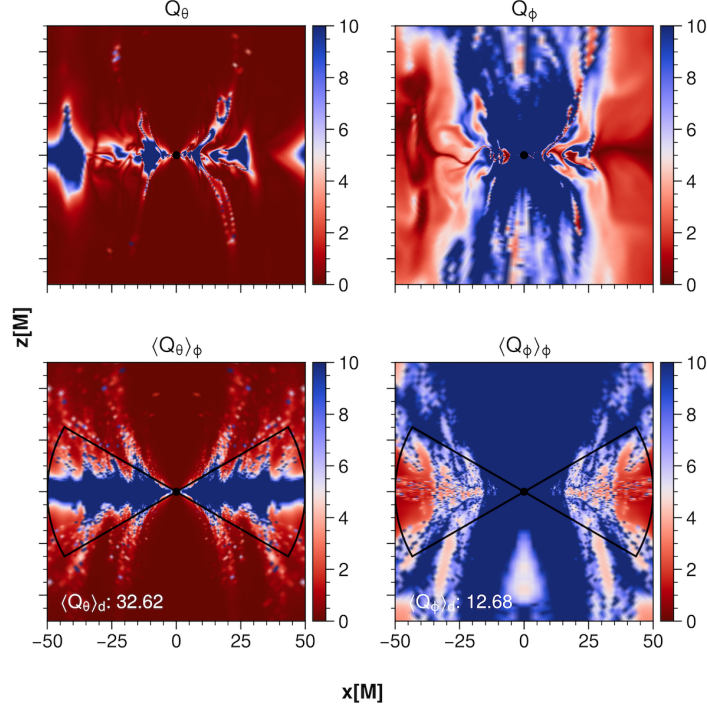


Fig. D.2. Meridional cross-section of MRI Quality factors in θ and ϕ directions. Top row: Meridional cross-section. Bottom row: Volume averaged Q-factors over the full azimuthal angle. The black lines indicate the regions where the disk is cut, poloidally, and subsequently averaged over the full azimuthal angle to obtain the disk averaged values given in the bottom left corners.

Appendix E: Error Estimation of Time Series

Here we elaborate on the error estimation of the correlated time series, inspired by Lalakos et al. (2025). The reduction of the number of independent samples can be quantified by the integrated autocorrelation time τ_{int} of a time series $f(t)$, which is defined as:

$$\tau_{\text{auto}} = \left(1 + 2 \sum_{k=1}^N \rho(k \Delta t) \right) \Delta t, \quad (\text{E.1})$$

where $\rho(t)$ is the normalized autocorrelation function of the unity normalized time series $f(t)$ at lag t , N is the number of samples and Δt is the sampling interval (5M in our case) for normalization. The normalized autocorrelation function is defined as:

$$\rho(k \Delta t) = \frac{1}{\sigma^2} \sum_{i=1}^{N-k \Delta t} (f(i \Delta t) - \mu)(f(i \Delta t + k \Delta t) - \mu). \quad (\text{E.2})$$

The autocorrelation function is computed up to a lag of $N/2$ to avoid noise-dominated estimates at large lags and normalized to lie between values of -1 and 1 to enable comparability between the simulations.

The error of the mean μ of a correlated time series of duration T is then given by:

$$\sigma_{\text{corr}} = \sigma \sqrt{\frac{2\tau_{\text{auto}}}{N}}, \quad (\text{E.3})$$

where σ is the standard deviation of the time series. We typically find values of $\tau_{\text{auto}} \lesssim 10M$ corresponding to an error $\lesssim 5$ higher than the standard error of the mean, when assuming the data is entirely uncorrelated. Therefore, we avoid underestimating the error of the mean.

Appendix F: Angularmomentum Fluxes at varying Radii

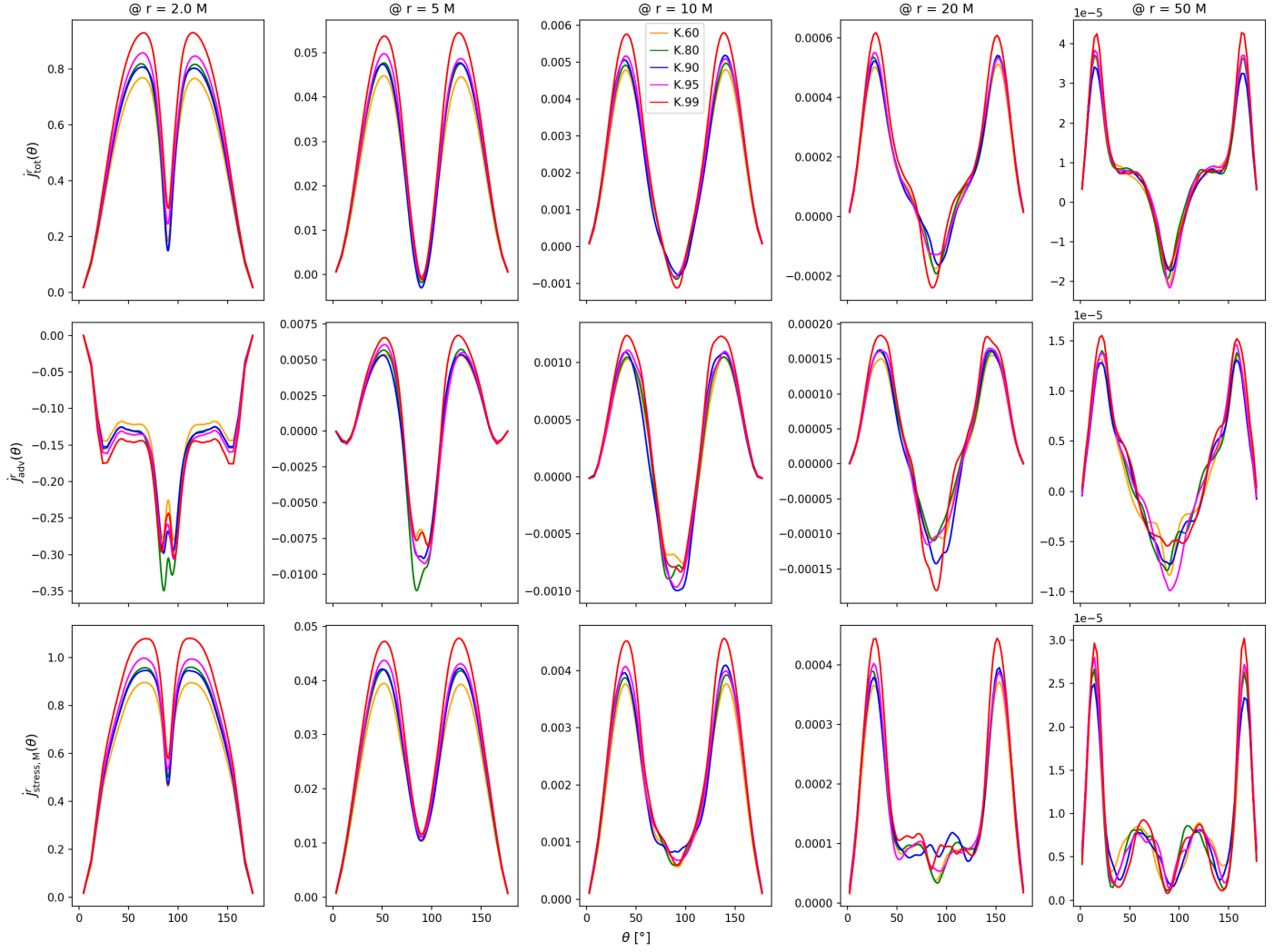


Fig. F.1. Polar slices of the radial angular momentum flux at varying radii increasing to the right. Solid lines are the radially outward flux and dashed lines are inward flux. Note the varying scales on the y-axis.

Appendix G: Morphology of a Flux Eruption Snapshot

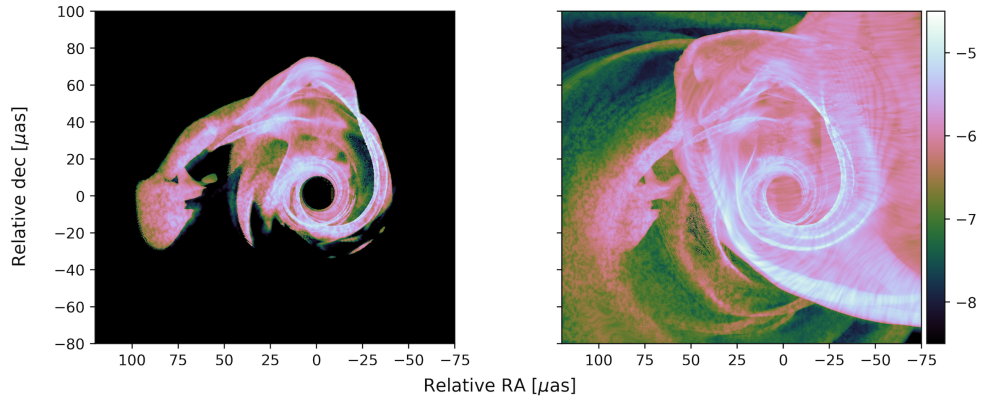


Fig. G.1. 86 GHz ray-tracings of the flux eruption of the K.99 run (same procedure as in Fig. 11 for the line integral convolution). Left image: only ray-traced thermal disk emission. Right image: ray-traced non-thermal jet and thermal disk emission